DEVELOPMENT OF A LOW-DOSE RADIATION THERAPY DEVICE FOR ACUTE RESPRITORY DISTRESS SYNDROME

A Thesis Presented for the

Master of Science

Degree

The University of Tennessee, Knoxville

Thomas Heath Davis

December 2022

ACKNOWLEDGEMENTS

Thank you to Dr. Eric Lukosi for his mentorship of myself from a young undergraduate to PhD student. Thank you to Brett Miller for his insight and advice pertaining to Medical Physics. I would also like to thank my family, Pam and Sarah Ellen, for their support over the last few years of study. Last, I would like to thank my fellow graduate students, Jake and Corey, for their friendship and especially their problem-solving skills.

ABSTRACT

This research focuses on the development of a low dose radiotherapy (LD-RT) device for treatment of acute respiratory distress syndrome (ARDS), a respiratory illness that affects millions of people a year. The use of orthovoltage (200 – 500 keV) X-ray energy provides many advantages over traditional radiotherapy delivery with linear accelerators, such as low cost and greater accessibility. In addition, X-ray tubes have been shown throughout history to provide good treatment outcomes for pneumonia, and research has shown LD-RT to be just as effective with ARDS. This proposal summarizes my efforts in determining the dosimetric properties of a LD-RT system to deliver treatment in a fast and effective manner. My research involves Monte Carlo transport simulations in MCNP to calculate the dose delivery and coverage of a whole lung treatment. In addition, different setup geometries and beam modifications will be explored to optimize the treatment delivery. The development of such a system would greatly expand the treatment options for ARDS type illness at a lower cost and greater accessibility than current radiotherapy options.

TABLE OF CONTENTS

LIST OF TABLES

LIST OF FIGURES

CHAPTER ONE

BACKGROUND INFORMATION

1.1 Introduction to Radiation Therapy

Radiation therapy (RT) has been in practice for a over century to treat diseases using radioactive sources, X-ray generation tubes, and particle accelerators. While the treatment methods have evolved with technology, the fundamental goal is to deliver energy in the form of radiation to induce a biological effect. This has made radiotherapy a valuable tool, especially in the oncology field for tumor control. Today, an estimated two-thirds of all cancer patients will receive RT as part of treatment [1]. Recently, the use of RT outside of oncology has regained the attention of the medical community. Studies early in the 20th century saw good results in the treatment of pneumonia and other respiratory illnesses, warranting a modern approach for low dose RT to treat disease [2-5]. This section will discuss the technological developments as well as clinical procedures that have shaped the radiotherapy field over the past century.

The discovery of X-rays by Wilhelm Rontgen in 1895 marks the beginning of scientific research in RT [6]. It was quickly discovered that prolonged exposure created inflammation, redness, and tissue damage on the skin. Prior to understanding these biological effects caused by radiation, within a year, the first X-ray treatments were carried out on patients, mainly for tumor control [7]. Around the same time, Marie and Pierre Curie started their research on natural sources of radiation leading to the emergence of brachytherapy with radium and other natural radioactive sources [8]. This allowed for more diverse treatment options due to the higher energy and intensity of these isotopes. Early X-ray tubes of the Crookes cold cathode design were limited in energy (<100 keV) and output resulting in limited tissue penetration and energy deposition rate. The therapeutic applications of X-rays were immediately recognized; however, their utility was initially limited to superficial skin cancers [1].

In 1905, reports from Musser and Edsall saw the potential for X-rays in low doses to treat pneumonia in a small study with five patients [9]. In their conclusion, they stated that further research was needed in order to properly understand the effects of RT. Almost 10 years later, a separate group of researchers, Quimby and Quimby successfully treated 12 cases of pneumonia with similar findings [10]. As was the case with Musser and Edsall, further research was warranted.

The introduction of orthovoltage (100 – 500 keV), Coolidge (hot cathode) X-ray tubes in the 1920's allowed a wider variety of treatments due to the increased penetration depth and higher X-ray output [11]. Around the same time (1924), Heidenhain and Fried released a larger study on pneumonia treatment with X-rays with more detailed findings. They showed that low doses of X-rays reduce inflammation of all types regardless of their location in the body. Further, this proved the clinical utility of treating deeper penetrating infections, such as pneumonia [12]. This study is generally considered to be the beginning of low-dose radiotherapy (LD-RT) for pulmonary type diseases, and many more pneumonia studies occurred in the following years. The authors McIntire and Smith, Scott, Solis-Cohen and Levine, Settle, Rousseau et al., and many others had shown similar good outcomes for patients suffering from unresolved pneumonia between 1924 and 1937 [13]. With the arrival of penicillin outperforming almost all other treatments, LD-RT research lost popularity. The use of LD-RT as a treatment option for pneumonia would never achieve broad support or scientific standing. This led to the use of LD-RT treatment for pneumonia all but disappearing from scientific studies in the early 1940's [13].

1.1.2 RT in the Megavoltage era (1940 - Present Day)

Many of the discoveries prior to 1940 serve as the foundation for what would be considered high dose RT used in oncology today. Hermann Joseph Muller's 1927 paper first recognized increased cancer risk and other genetic effects due to radiation exposure [14]. This discovery coincided with the work of Henri Coutard, a French radiologist, who first demonstrated in 1922 that X-ray doses which would be intolerable for a single treatment, when spread over multiple days, had no effect on subcutaneous tissues [15]. This

work led to a fractionated treatment process whereby the dose is divided into multiple smaller “fractions” to promote healthy cell repopulation. This method was adopted worldwide in 1935 and is still the basis for most radiation therapy planning today.

By the end of the 1930’s, X-ray tubes were able to produce energy in the MeV range, increasing the depth and uniformity of treatment marking the beginning of the megavoltage era of RT [1]. These efforts to continually increase energy led to the adoption of other accelerator devices such as the Van de Graaff generator, an electrostatic generator, originally developed for particle physics. It is capable of accelerating electrons in the 1-2 MeV range. The first installation of a Van de Graaff generator was in 1937 at Huntington Memorial Hospital in Boston [16]. Another accelerator device adopted from the physics community was the betatron which accelerated electrons to MeV energies by injecting them into a doughnut shaped tube and used alternating magnetic fields to accelerate. These early betatrons were capable of energies up to 50 MeV [17].

With the development of the nuclear reactor in the early 1940’s, a new method of delivering higher energy radiation therapy was now possible due to Cobalt-60 and other isotopes. With X-ray tubes, Van de Graaff generators, and later linear accelerators (linacs), electrons are accelerated into a dense metal target to make X-rays. Betatrons, unlike the other devices, were primarily used for direct beta (electron) treatment, not X-ray production. With isotopes, gamma rays, which are photons just like X-rays, come from the radioactive decay of the nucleus. The isotope Co-60 has a 1.17 and 1.33 MeV gamma ray, perfect for deep penetration, and by collimating large amounts of this isotope in a device, it can be used for high energy RT. In 1948, the first cobalt therapy device was licensed by the Atomic Energy Commission, nicknamed “cobalt bomb,” to Dr. Harold E. Johns who would complete the first treatment in 1951 [18].

Another advancement during World War two was the invention of high-frequency, high power microwave generators to be used in radar systems. With the addition of a wave guide, the first linear accelerator or linacs were developed with the ability to create X-rays from 2 to 25 MeV with the first device installed in 1953 at Christie Hospital in Manchester, United Kingdom. Later developments of the linac allowed for the use of both electrons and X-rays at different energies from the same machine [19]. For these reasons, by the 1970s,

the medical linac had become the work horse of radiotherapy offering a range of treatment energies from 2 MeV to 25 MeV.

The steady increase in treatment energy into the MeV range after the 1940's presented many challenges, especially when it came to targeting structures and calculating the dose to a patient. This changed with the introduction of the CT-scanner in the early 1970's [20]. Prior to this, treatment plans were calculated to single points in the body using physical measurements of the patient with a combination of radiographs to locate the treatment points. In the late 60's, early computer programs were used to calculate these 2D treatment plans, but with the CT scan, 3D visualization of the body and organs of interest was finally possible [21]. These treatment plans allowed for better patient alignment, dose optimization, but most importantly, the precise visualization of target structures and normal tissues in the patient to deliver high dose rate therapy (HD-RT).

1.2 LD-RT Delivery for ARDS

Recently, the use of LD-RT for treatment of respiratory diseases became more attractive to healthcare providers worldwide due to the onset of the SARS-CoV-2, commonly referred to as COVID-19, pandemic. Acute respiratory distress syndrome (ARDS) is a pulmonary condition that results in low blood oxygen levels in the affected patient. It can be brought on by many factors such as bacterial/viral infections, trauma, sepsis, and/or drug overdose, however, bacterial, and viral pneumonia are the most common causes [5, 22]. Acute inflammation of the lungs results in low blood oxygen levels and this inflammation is exacerbated by the influx of cytokines and other inflammatory compounds. This response can lead to multiple organ disfunction syndrome with long term physical and psychological effects. A 2016 study across 50 countries identified that 10.4% of ICU patients met ARDS criteria and among the severe cases, the mortality rate was 46% [23]. This indicates that an alternative, generalized treatment of ARDS would benefit the medical community.

With COVID-19, the danger of ARDS type illness received worldwide attention with many treatment modalities being investigated to suppress ARDS symptoms. The most

severe complications leaned heavily towards those of advanced age and/or those with comorbidities [24]. Early on, emergency use authorizations had been given in the USA for treatments with remdesivir and dexamethasone. The World Health Organization Solidarity Trial negated benefits to many of the commonly used anti-viral regimens. The initial lack of efficacy for drug-based treatments was akin to the pre-antibiotic days of the early 20th century. Many researchers looked to historical treatment of bacterial/viral pneumonia with LD-RT, as discussed previously [13, 25].

Multiple groups have shown the efficacy of LD-RT for the treatment of COVID-19 induced ARDS. One such group demonstrated that an acute X-ray dose of 150 centi-gray (cGy) to the bilateral lungs resulted in a marked improvement in 4 of the 5 patients treated, even with an advanced age (median age 90). They noted that low-dose whole-lung radiation led to rapid improvement without acute toxicity [2, 3]. Data from Tehran indicated similar results with patients receiving 0.5 Gy whole lung irradiation resulting an 80% recovery rate with no acute toxicity [26]. A study from Madrid, also noted good results with 7 of the 9 patients being discharged [27].

These studies have demonstrated that LD-RT has an anti-inflammatory effect by altering the function of a variety of inflammatory cells. Cytokine Release Syndrome (CRS) or “cytokine storm” is the rapid increase of pro-inflammatory cytokines, and in COVID-19, macrophages are an important component of this immune system response [4]. The release of macrophages promote recovery by fighting infection and the stimulation of other immune cells. With CRS, the sudden influx of macrophages can overwhelm the lungs with inflammation caused specifically by the M1-like phenotype, a pro-inflammatory macrophage. One reported mechanism suggests that LD-RT polarizes macrophages towards M2-like phenotypes which are anti-inflammatory in nature [4, 25]. Adjusting the ratio of pro-inflammatory M1-like phenotypes towards the anti-inflammatory M2-like phenotypes can improve this auto-immune response. Clinical data suggests that whole lung dose in the range of 0.3 – 1.5 Gy can induce the desired effect in limiting the cytokine storm and neutralizing inflammatory factors in CRS. These proposed mechanisms involving the modification of cytokines, the historical treatment of pneumonia, and

preclinical mouse studies all suggest that LD-RT is a viable, general treatment for ARDS type illness [28].

In all the studies of LD-RT for ARDS treatment, medical linear accelerators (linacs) were used for treatment delivery [2-4, 22, 25]. Today, they are the most common RT device and can be found in nearly every radiation oncology department in the country [29]. While they are more than capable of delivering precise whole-lung LD-RT for ARDS in a timely manner, there are some logistical and financial drawbacks for their large-scale adoption for this treatment.

In nearly all cases, ARDS patients are located in the intensive care unit (ICU). If immediate treatment is necessary, they would be transferred to the radiation oncology department, where they would likely need a CT scan for planning prior to treatment. This is common today, where patients are brought in with little to no notice in order to receive palliative treatment. However, if general LD-RT were to become a common occurrence, the increased workload could strain the RT department. This would be exacerbated if the department was already operating at maximum capacity. With severe cases of ARDS, LD-RT may be needed immediately before worsening of the cytokine storm [25]. This includes nights and weekends when most RT departments are not typically staffed.

The addition of another linac could meet this increased demand, however, linacs are extremely expensive (millions of dollars). Due to their high X-ray energies, they require radiation vaults with many feet of concrete for shielding the staff and public. This increases the associated costs and puts a logistical strain on hospitals where space is limited. Whole lung LD-RT is also a simple treatment protocol. The upper limit of dose required for LD-RT is 1.5 Gy, approximately equal to 1 fraction of the typical 40 prescribed for lung cancer [30]. The low dose and simple setup would not warrant many of the features available with a modern linac such as intensity-modulated radiation therapy (IMRT), volumetric modulated arc therapy (VMAT), or image-guided radiation therapy (IGRT) [31]. Therefore, the cost of LD-RT using a linac would be unnecessarily high, in order to pay for the overhead associated with these advanced features.

This leads into the biggest problem, most hospitals in the country do not have a radiation oncology department. A 2006 study identified that only 20% of U.S. hospitals

have a medical linac [32]. Small rural hospitals do not have the financial incentive or patient load to necessitate the investment into radiation oncology. In this case, patients who could potentially benefit from LD-RT for ARDS treatment would need to be transported to a different hospital which may cause further deterioration of their condition. In the case of the COVID-19 pandemic, patient transport was not an option due to the overfilled status of the hospital system worldwide.

Looking to history, the X-ray tube was more than adequate to deliver LD-RT for the treatment of pneumonia. While modern medicine has relegated their use to imaging, orthovoltage tubes are more than capable of producing sufficient energy and fluxes for LD-RT. Because of their simplicity and lower operating potential, they are orders of magnitude cheaper than medical linacs (tens of thousands of dollars). Their much lower beam energy further reduces shielding requirements and associated costs. We propose that a modern radiotherapy device, using orthovoltage X-ray tube energies, be developed to deliver LD-RT for ARDS. This system would benefit from greater hospital availability for treatment, regardless of a radiation oncology department with traditional RT systems.

1.2.1 LD-RT Risks

One concern using LD-RT for respiratory illness is the potential for developing cancer later in life. The occurrence of radiation induced second malignancies (RISM) depends on factors such as lifestyle, treatment modality, and genetic predisposition [33]. How each of these factors contribute to RISM is difficult to differentiate, but age is a good indicator of the total risk. Children and younger adults are more likely to survive for a longer period of time following RT, therefore they have the greatest risk of RISM. The Childhood Cancer Survivor Study has shown that after 30 years, treatment related mortality attributable to secondary tumor formation does increase [34].

The increased risk of RISM lung cancers following HD-RT treatment of Hodgkin Lymphoma has been determined in other epidemiological studies. With a median age of exposure of 49-50 years, the estimated Excess Relative Risk (ERR), defined in Equation 1, per gray was found to be 0.15 [35].

$$ERR = \frac{R_e}{R_u} - 1 \quad (1)$$

ERR is defined as the rate of the radiation-induced disease R_e, divided by the rate of the disease in the unexposed population R_u, minus 1. While this risk is normalized to Gy received during treatment, cumulative doses may reach 15 to 70 Gy which may not represent the ERR of LD-RT accurately.

Another epidemiological study following the health effects of low-level radiation is the Million Person Study (MPS). It has been underway for the last quarter century following the health effects of radiation workers and veterans [36]. The ERR per 100 mGy for radiogenic lung cancer over 915,543 people is 0.042. This result would indicate that the general population lung cancer rate of 7% would increase to 8.47% following 0.5 Gy LD-RT treatment. The upper bound treatment dose of 1.5 Gy would result in a cancer rate of 11.41% [37].

Both studies suggest that the ERR of lung cancers following the administration of LD-RT is low. The highest single fraction dose of 1.5 Gy would only increase the lung cancer rate from 7% to 11.41%. However, further research of LD-RT for ARDS may suggest that lower clinical doses achieve the desired effect. This would further reduce the ERR of tumor formation from treatment. Evidence from the COVID-19 pandemic suggests that patients of advanced age or with comorbidities often suffered the most severe ARDS symptoms when drug treatment methods failed. As previously suggested, older patients have a lower chance of RISM due to their shorter projected life span, therefore, the benefits of LD-RT may outweigh the small increased risk of long-term cancer formation.

1.3 Radiation Interactions in the Body

It is important to understand how radiation interacts in the body in order to determine the effectiveness of a treatment modality. When ionizing or indirectly ionizing radiation interacts with tissue, it will deliver energy which can weaken or kill cells. This is

defined by the dose unit Gray (Gy) in Equation 2, which represents the amount of energy delivered to a particular mass of tissue or material.

$$D = \frac{Energy\ Depostion}{Mass\ of\ Medium} \tag{2}$$

In this function, the amount of energy delivered is in Joules (J), and is divided by the mass of the medium in kilograms (kg) [38]. If the volume and density of a particular tissue is known, then the mass can be calculated.

The dose delivered from an MeV linac or an orthovoltage X-ray tube is the same if the energy deposited in a given mass is the same. This function gives a convenient method for comparing the treatment performance of different sources since the biological response of cells is related to the amount of dose given. For X-ray sources, dose response depends on the individual atomic interactions between incoming X-rays and the atoms composing the cell. When an incoming photon interacts in a medium, it deposits energy in one of three main ways depicted in Figure 1.

The first method is through the photoelectric effect process where incoming photons will strike an electron in the shell of an atom. If the photon energy is higher than the electron binding energy, it can be ejected from its orbital shell with the energy of the incident photon. In this interaction, the photon is completely absorbed [39]. This is considered a low energy phenomenon and is more prevalent with high-Z materials such as metals.

The second interaction type is Compton scattering which occurs when the incoming photon is scattered off a free electron in the tissue. The scattered electron energy is a function of the incoming photon energy and the angle at which it scattered [40]. The energy transferred to the electron is maximum when the angle between the scattered photon and the direction of travel is 180° (scattering directly backwards). Compton scattering is the most common interaction with orthovoltage to MeV photon energies.

The last method of interaction is through pair production. This happens when an incoming photon energy has more than two times the rest mass of an electron, 1.022 MeV.

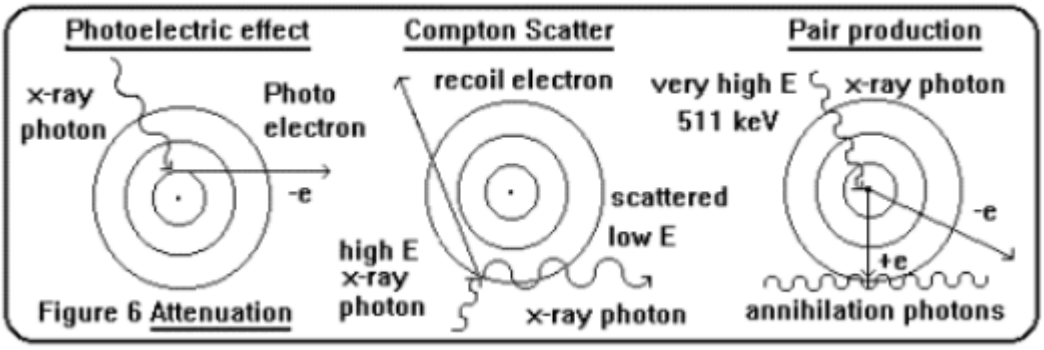

Figure 1. Illustration of the three main modes of photon interactions resulting in energy deposition in the body [41].

The photon is absorbed by the nucleus of an atom, creating an electron/positron pair. The energy of the photon will be reduced by 1.022 MeV, and when the electron/positron pair annihilate, two 0.511 MeV gamma-rays will be produced. This cannot occur below the 1.022 MeV threshold and does not become common inside human tissue until the photon energy reaches the multiple MeV range. At very high photon energies (above 10 MeV) photonuclear interactions are possible where the nucleus absorbs the proton and a proton or neutron is ejected, however, this reaction is rare and usually ignored.

In the human body, the photoelectric effect and Compton scattering are the dominant modes by which photons interact. Both cause an electron to ionize or break out of the orbital shell. If this electron was involved in a bond between two atoms, it will break this bond, ejecting the electron. Secondary effects are caused by the ejected electron striking other bonded electrons freeing them. This cascade of electron ejections from a primary interaction are called delta electrons and can cause many more bond breaks than the initial interaction.

If the break occurs in the DNA strand, this can trigger a wide range of effects. Depending on the cell type and where the break occurs, this can either be repaired or in other cases, trigger apoptosis where the cell intentionally dies. Another potential outcome following a DNA break is reproductive failure of the cell [42]. The likelihood of one outcome versus the other is chiefly determined by the radiosensitivity of the cell.

Another outcome of radiation exposure is the production of free radicles inside the tissue. The most damaging is the hydroxyl radicle (OH-) which can break multiple bonds (especially DNA bonds) over its very short lifetime of 10E-5 seconds. These can be formed by the primary interaction of X-rays, or from the cascade of secondary delta electrons. Nearly two-thirds of radiation induced damage from X-rays and gamma-rays are from indirect, free radicle formations [43]. The probability of any of these effects weakening or killing cells increase as the dose increases. They also increase with the energy of the primary X-ray due to the differences in delta electron track structures. High energy X-rays create many more delta electrons, even with the same dose delivered as low energy X-rays,

however, this is outside the scope of this discussion. In RT, dose delivered is the driving factor in achieving the desired cellular response.

These interactions have a strong effect on RT delivery other than determining energy deposited in tissue. As a photon beam passes through tissue, these interactions both absorb photons and change their energy through scattering. The combination of these effects as a function of distance in a material is quantified by the mass attenuation coefficient [44]. This value relates how quickly photons will be stopped due to absorption, scattering, etc. as a function of energy and distance. Figure 2 shows that in water, an analogous material to human tissue, the attenuation decreases with energy. This explains why MeV beams are used to increase the uniformity of dose at greater depths. The mass attenuation coefficient is lower, and the penetration of these X-rays is higher, leading to decreased dose drop-off.

The poly-energetic nature of radiation from X-ray tube and linac sources means that the attenuation of an X-ray beam is a convolution of the X-ray output energy spectrum and the mass attenuation across all energies of that spectrum. Because of the higher attenuation of low energy photons, the output energy spectrum changes as the X-rays pass through a material. Initially, low energy X-rays with high attenuation coefficients will stop faster resulting in higher dose rates closer to the surface. This shifts the average energy of the X-ray spectrum towards a higher energy as the X-rays pass through the body. In MeV beams, this issue is less pronounced due to the high average spectrum energy. With orthovoltage X-ray tubes, this effect must be accounted for in dose calculations.

While these factors make understanding the X-ray intensity (flux) and energy spectrum through a material challenging, another compounding factor is the divergence of the beam. The area in which X-rays are produced in the target is considered a point source. The total X-ray intensity across all energies decreases proportionally to the distance to this point, squared. The combination of these effects determines the photon flux available to deliver energy to tissue at a given depth. Further, the energy of the photons determines the type of interaction they will undergo based on the cross-section (photoelectric, Compton scattering, pair production), and how much energy these interactions will deposit into the medium.

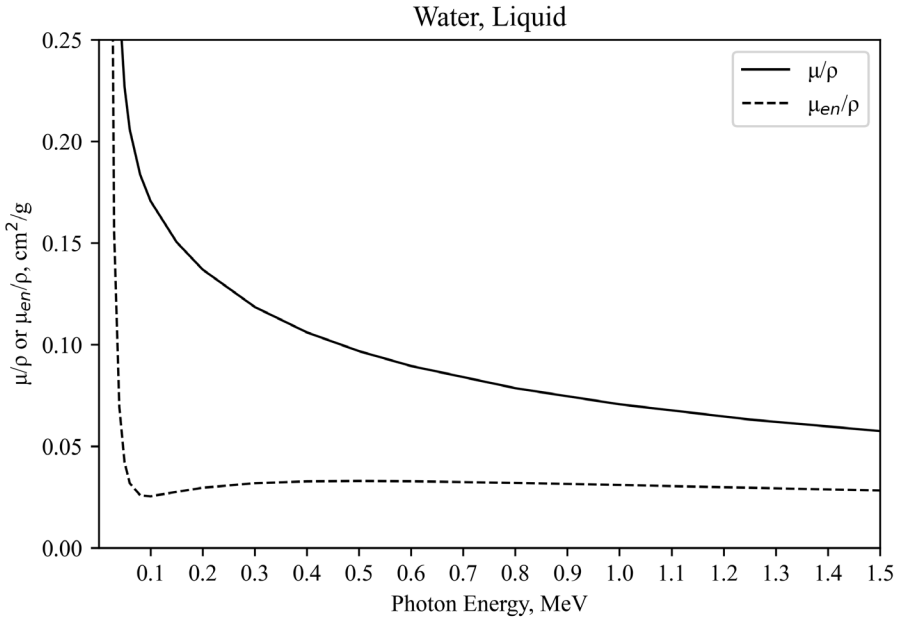

Figure 2. Plot of the mass attenuation and energy attenuation coefficients as a function of photon energy in MeV [45].

To determine dose to the lungs accurately, we must calculate the photon flux, photon energy and how much energy is deposited through the body. This is complicated given that each of these variables change as a function of depth. Further, the human body is comprised of many different tissue types, all with different interaction probabilities and densities, which alter how each of these variables change along each path length.

1.4 Fundamentals of Radiation Production

Since we are interested in delivering LD-RT with an X-ray tube as opposed to a medical linac, it is important to understand how they produce X-rays. With any medical X-ray producing device, the principle of operation is largely the same. Electrons are accelerated until they possess a very high kinetic energy and directed into a dense, high-Z material. Inside this material, X-rays are produced through two interaction mechanisms [46]. The first, and most common interaction being bremsstrahlung radiation or "braking radiation". Bremsstrahlung arises from the acceleration or deceleration of a free electron in the field of a nucleus. The loss of kinetic energy by the free electron is given off in the form of electromagnetic radiation, i.e., photons, thus satisfying the law of conservation of energy [47]. The reason high-Z materials are used is because bremsstrahlung yield is proportional to the atomic number of the material used, as described by Equation 3.

$$Y \sim ZT^2 \tag{3}$$

In this equation, Y is the relative radiation yield, T is the kinetic energy of the incoming free electron, and Z is the atomic number of the target material. It is common for the target in any X-ray producing machine to be a very heavy, dense metal such as tungsten or a similar alloy. This is done to increase the proportion of X-rays produced for a given number of incoming free electrons. The kinetic energy, T, of the electron is determined by the accelerator design and the amount of energy the device can transfer to the electrons. The maximum output X-ray energy from the device will be equal to the kinetic energy, T, of the electron. This is the potential difference of an X-ray tube, usually referred to as kVp,

the peak acceleration voltage in units of kiloelectron volts (kV). It is important to note that not all the kinetic energy is converted into X-rays. Even in MeV accelerators, only a few percent of the electron's kinetic energy is converted into photons. This conversion is even lower for low energy accelerators, like X-ray tubes. Most of the energy is released into the target in the form of heat [46].

Some important features of bremsstrahlung radiation are the strong directional dependance and poly-energetic nature of the X-rays produced. As higher electron energies are used, the higher energy X-rays become more forward directed. This has a direct effect on the design of radiotherapy devices, as well as their limitations. In Figure 3, the angular dependence as a function of energy is illustrated for different electron energies. X-rays generated in the lower end of orthovoltage energies (100-500 keV) have a near equal distribution in all directions (4π distribution) relative to the electron beam, however, this becomes skewed forward at the higher end [48]. In the MeV range, the X-ray production is nearly all in the forward direction. This phenomenon is explained by the conservation of momentum of the electron/nucleus/X-ray pair. The higher the kinetic energy of an electron, the higher the momentum in the forward direction. In a three-body problem such as this, the more forward directed the X-ray must be to satisfy the laws of conservation of energy and momentum [49].

The poly-energetic nature of these X-rays stems from the way in which electrons slow down in a material. While all incoming electrons possess the same kinetic energy, they each undergo different interactions. Electrons that travel closer to a nucleus of the target material experience a stronger force, therefore, a greater deflection toward the nucleus and change in kinetic energy [46, 49]. The resulting X-ray will possess this change in electron kinetic energy. Rarely, electrons will lose all their energy in one interaction, resulting in an X-ray energy equal to T. In most cases only a portion of its energy is lost as an X-ray leaving the electron with a fraction of its initial energy. It is then free to continue to interact with another nucleus, repeating the process. Most electrons undergo multiple interactions before stopping and this statistical nature of interaction leads to a characteristic poly-energetic X-ray spectrum seen in Figure 4. It shows a decrease in X-ray intensity from 0-50 keV which is a product of the anode and tube design [50].

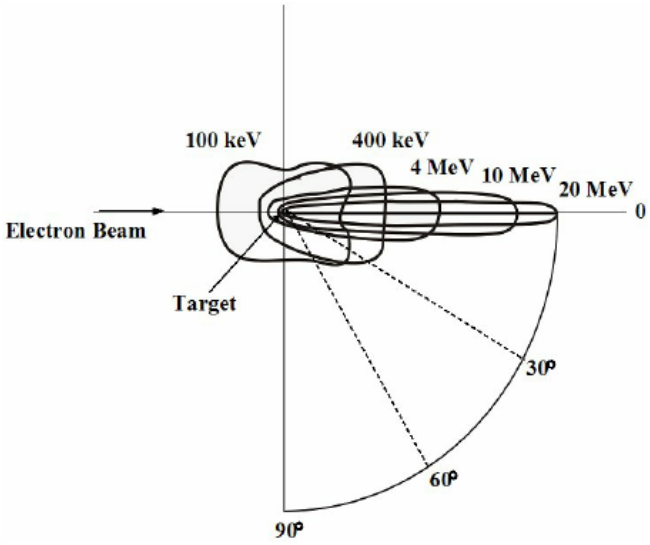

Figure 3. An illustration representing the angular dependance of bremsstrahlung X-rays as a function of angle and energy from an incident electron beam [48].

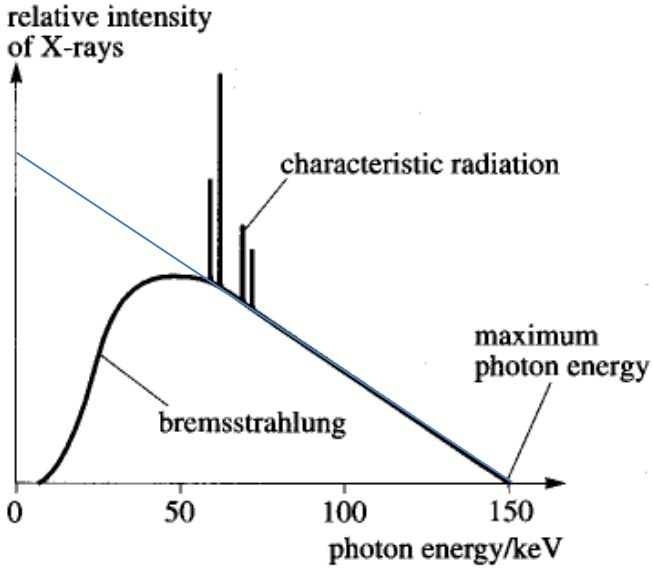

Figure 4. Illustration of bremsstrahlung X-ray Spectrum as a function of energy and intensity. The characteristic X-rays are a product of the target material electron orbital energies. The maximum energy in this representation is 150 keV but the spectrum shape would be the same at any acceleration energy [50].

The intensity of X-rays produced would match that of the blue line, however, since electrons penetrate the anode a short distance, low energy X-rays produced there do not possess enough energy to exit the material. This X-ray spectrum represents a device with a 150 kV acceleration potential where the maximum photon energy matches this at 150 keV. The trend of this spectrum would be the same regardless of the acceleration potential of the device, with the maximum photon energy equal to the acceleration potential.

The second form of X-ray production inside of a target is in the form of characteristic X-rays as seen in Figure 4. These are emitted from high-Z elements when their orbital electrons transition between atomic energy levels [46]. These occur when there is an electron vacancy in the K shell or n=1 energy level of the atom. This is caused by the incoming electrons ejecting these inner shell electrons. It can also be caused by photelectric ejection or Compton scattering from X-rays of these K shell electrons. Subsequently, electrons in the n=2 and n=3 energy levels can transition to the n=1 state emitting an X-ray equal to the energy difference of the levels. These are referred to as K-α and K-β characteristic X-rays and their energy is dependent on the nucleus of the target (energy level separation).

1.4.1 X-ray Tube Operating Principles

Early X-ray tubes, from the early Crooks tube to modern rotating anode tubes, all operate using an electrical potential difference from the cathode (-) to the anode (+) [51]. The potential difference between the two is measured in electron volts (eV) and the kinetic energy of the electrons accelerated between the two is equal to this potential difference. A 100 keV tube has an electron energy of 100,000 eV when it strikes the target anode. This takes place inside of a vacuum chamber or tube (hence the name X-ray tube) so the electrons can accelerate unimpeded by air or other gases [51]. Early designs generated electrons through the ionization of residual gases inside the tube or trapped in the cathode for acceleration and are referred to as cold cathode tubes. Later designs such as hot cathode tubes which use thermionic emission of electrons from a tungsten filament heated with

electrical current [52]. Thermionic emission is the release of electrons as an effect of high temperature and greatly increases the number of free electrons to be accelerated [53].

The number of electrons to be accelerated in a tube is referred to as tube current and is limited primarily by the thermal heating of the target anode [51]. These targets can quickly reach thousands of degrees Celsius, and unless steps are taken to cool the target, or the tube current is reduced, the target will melt. For imaging, small electron focal spot sizes are necessary for good image quality, further increasing the heat load per unit area. To overcome this, while increasing the current and X-ray output, more complex cooling systems and anode designs have been developed. Rotating anode tubes utilize larger, disk-shaped targets that are rotated at very high speeds to spread the heat load from the electron beam over a larger area. Cooling liquid, typically oil, is also used to further draw heat from the anode to be dissipated through radiators or other heat exchangers away from the X-ray tube [51]. Rotating anode tubes are commonly used in CT scanners, radiography, and fluoroscopy machines where size is limited, and the focal spot sizes are small. When focal spot sizes are larger, heat dissipation can be handled sufficiently by air or water-cooled heat sinks with fixed, non-rotating anode targets.

The X-ray output of these tubes are typically 90º to the electron beam. At orthovoltage energies, the angular distribution of X-rays is still mostly symmetrical around the target with some forward biasing at higher energies. This means that the X-ray intensity at 90º is nearly the same as the forward direction. However, the anode itself is a dense piece of metal which can self-shield the X-rays produced since they then would have to travel through the target. With variable energy tubes, this would be nearly impossible since the target thickness would need to be optimized for each energy independently. Locating the beam port perpendicular to the electron beam is a simple way to overcome this limitation with little complexity. Angled anodes are also utilized to increase X-ray beam uniformity along the beam axis. By angling the anode toward the beam port, X-rays produced shortly inside the anode face have less anode material in their path towards the port. However, this does not entirely resolve the issue. As the angle of the X-ray becomes closer to parallel with the anode face, it travels through more material. This creates an effect known as the

heel of the beam, where the X-ray intensity decreases toward the front of the beam, parallel with the anode face.

Another design consideration for X-ray tubes is the use of beam filters. Filters can be used to increase the effective energy of the X-ray beam by blocking low energy X-rays. This is called beam hardening and while it does decrease the total output intensity across all energies, it biases the spectrum toward the higher end which is very useful in imaging and LD-RT therapy with X-ray tubes [54]. Characteristic X-ray peaks can also be "filtered". This can be accomplished with layers of low-Z metals or alloys that will block the characteristic X-rays of the previous material until they are no longer present in the spectrum [55].

1.5 Dose Calculation Methods

In radiotherapy, many different algorithms can be used to calculate the dose delivered to a patient. This begins with a CT-scan of the target region which gives an approximation of the density and attenuation coefficient for each voxel. The simplest calculation methods involve point calculation of dose by approximating pencil beams moving through the voxels [56]. More complex algorithms use a method known as convolution-superposition. This involves many beamlets simulated moving through each voxel where primary beam dose and scatter fractions from surrounding voxels are calculated [57]. These methods involve multigroup energy and tissue calculations to analytically solve the dose delivered to a patient. They depend on accurate beam data to match the expected output from the RT device [58]. Lookup tables supply many factors such as beam profile, X-ray attenuation coefficients and X-ray scattering factors to approximate the complex physics of radiation interaction.

These analytical methods are employed to simplify the dose calculation and to speed up RT planning. However, they are only an approximation of true radiation transport and may still contain errors. Monte Carlo simulations of the dose delivery results in the highest dose calculation accuracy. This method of dose calculation is very computationally expensive, but it does have its uses in modern RT planning [59].

Monte Carlo simulation is a valuable tool in nuclear engineering, high energy physics and RT dosimetry. These simulations utilize probabilistic calculations of many discrete, random events which in aggregate forecast useful results. In the case of dosimetry, Monte Carlo methods can simulate individual particles with random trajectories traveling through a defined material. At each point in the material, the probability of a particle event is calculated and assigned to the simulated particle based on cross-section tables, equations, and many other sources of nuclear data [60]. Monte Carlo simulations are considered the closest approximation of true radiation transport and are the most accurate method of determining dose. These models are computationally expensive since particles must be simulated as moving through the material with calculations performed at each step.

The Monte Carlo program MCNP6.2 (Monte Carlo N-Particle) from Los Alamos National Laboratory was selected for its familiarity and long-standing history inside the nuclear engineering and medical physics communities. For complex simulations involving dosimetry, many particles must be simulated for the desired result, dose, to converge. Convergence in MCNP means that the specified tally region/volume/tissue has had enough particle interactions such that the tally result approaches the mean [61].

1.5.1 Phantom and Beam Modeling

The method for determining the treatment capabilities of the LD-RT system utilizes MCNP simulation of the entire particle transport process. By simulating every step in the X-ray generation process from electron to X-ray to the body, a working model can be developed. This is used to accurately calculate the dose delivered to a human phantom. MCNP is unable to import CT-scan data as a reference body for dose calculations. Instead, VIP-man phantom will be used which is a voxelized (tomographic) phantom developed from segmented cadaver images obtained from the Visible Human Project [62]. This phantom is composed of 5,941,740 voxels, each 4 × 4 × 4 mm in size. These voxels each contain a material composition closely approximating over 60 different tissue types and are placed inside the simulation space to make a standard adult male phantom.

With the goal of delivering 1.5 Gy to the isocenter of the lungs, a working beam model must first be developed in MCNP. All X-ray tubes of this energy range have similar operational characteristics with similar anode (target) materials, and X-ray ports 90 degrees to the electron beam. They differ in beam port size, acceleration potential (kVp), and tube current (mA), all which effect dose uniformity and treatment times. The acceleration potential (tube energy) has the greatest effect on dose uniformity due to better penetration with energy and must be determined to meet treatment protocols. Our beam simulations are based on the COMET EVO300D which is capable of 300 kVp at 3 mA which should result in acceptable treatment times and dose uniformity. However, should a different tube design or acceleration be needed, only a few parameters would need to be changed.

The value of VIP-man for evaluating LD-RT lies in the user ability to specify regions to calculate energy deposition. MCNP delivers energy deposition in MeV/g which can quickly be converted to Joule/Kg or Gy. By specifying the organs of interest such as skin, heart, bone, and especially lung within the treatment field, the dose delivered can quickly be determined in a simulation run. Alterations to the beam can be made with the addition of filters, or alternate setup geometries to adjust the dose distributions for better coverage and uniformity.

CHAPTER TWO

PROPOSED RESEARCH

The proposed thesis seeks to prove the viability of low dose radiotherapy (LD-RT) with orthovoltage X-ray tube energies of 300 keV or lower for the treatment of acute respiratory distress syndrome (ARDS). Such a device would offer whole lung LD-RT up to 1.5 Gy in a fast and efficient manner while minimizing dose to non-target tissue. As discussed in Chapter 1, LD-RT has shown good results in the treatment of ARDS, especially in emergency/severe cases. However, widespread adoption of LD-RT is currently limited by linac availability and large operational costs. This system would address both issues by increasing the hospital availability through a combination of much lower technology costs and lower operational energy, not requiring linac vault levels of shielding.

First, I will develop an accurate beam model of an orthovoltage X-ray tube in MCNP. This model will be based on the engineering specifications of the selected COMET EVO300D X-ray tube and will be adjusted until the simulated output matches that of the provided documentation. This beam model can then be used in conjunction with a human phantom model in MCNP to determine the coverage and dose to the lungs as well as other organs at risk in the field. Different setups, such as anterior-posterior or posterior-anterior fields, will be evaluated as well as combinations of the two. Additionally, different filter designs will be evaluated to achieve homogeneous dose distributions in the shortest exposure time possible.

Second, I will experimentally evaluate the performance of the simulation with a human phantom inside of a testing enclosure with imbedded dosimetry sensors. It is important to determine if there are any inconsistencies with the model and the true dosimetry results. Corrections can then be made so that the true beam and simulated beam agree.

Third, we will use the simulated and experimental beam results to develop a LD-RT treatment planning protocol that does not rely on a MCNP simulation of every setup. Prior to the invention of the CT scanner, radiographs along with simple point calculations

were used for planning, which we intend to do here. A combination of radiographs and simple measurements along with the large open field design of this system will allow for this type of planning. This planning model will be compared against the simulation and experimental results to test its validity in LD-RT planning for whole lung treatment.

CHAPTER THREE

CURRENT PROGRESS

3.1 X-ray Beam Modeling

We found early on that simulating the electron beam/target/X-ray system with the VIP-man model, required run times lasting multiple days to a week to get good dosimetry results. The complexity of the phantom model with the increased computational expense of tracking electrons and photons in the same simulation drastically reduced the computational speeds. This is compounded by the bremsstrahlung X-ray conversion rate of less than 1%. Both factors resulted in a low number of electron simulations per hour and orders of magnitude lower X-ray generation rates, therefore, long dose rate convergence times. This made iteration of the model slow, and any mistakes made with a setup would waste far too much time. The decision was made to model the beam outside of the phantom simulation and create an X-ray source for use with VIP-man.

The creation of the beam model started with MCNP simulation of a simplified X-ray tube. This consisted of a target anode made of tungsten and a 1mm Ø electron beam incident on the anode in vacuum. The anode was made many cm thick and angled 20-degrees to the electron beam as shown in Figure 5 so that: 1) electrons will not penetrate through the anode and 2) the bremsstrahlung X-rays can escape due to the angled face. This design was the same as the source used in the original slow simulation but without any other structures. As shown in Figure 5, a tallying surface utilizing an FMESH was placed at 100 cm, perpendicular to the point the electron beam strikes the target. The area of this round surface was 6,962 cm^2 corresponding to an X-ray beam half angle opening of 27 degrees. This was chosen to roughly match the solid angle of the COMET EVO300D with a $40° \times 60°$ opening angle. The X-ray flux in particles/cm^2 and energy in 1 keV bins was recorded on the tally surface as seen in Figure 5. The total fraction of X-rays that cross this surface divided by the number of electrons generated in the beam gives the bremsstrahlung X-ray production factor of 0.002448 X-rays/electron.

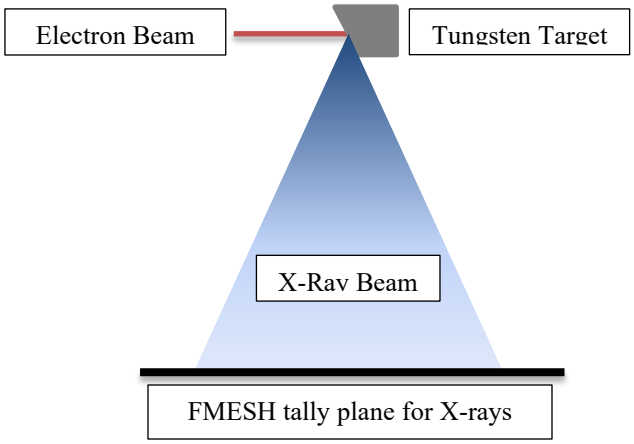

Figure 5. An illustration of the X-ray simulation with the electron beam, tungsten target, X-ray beam and tally surface depicted. While not illustrated, the beam expands in all three dimensions from the target to the tally surface.

Next, a new X-ray source was made by normalizing the flux per 1 keV energy bin to act as the probability of emission for each energy. The source was set so that every X-ray was generated at a single point with a random vector bounded by the 27º half angle cone, further increasing calculation efficiency by only simulating photons traveling toward the chest of the phantom. The weight of each photon generated was also increased by the inverse of the solid angle, 18.05, since MCNP normalizes to 4π sr by default. The main goal of this new source was to increase simulation speed which it accomplished, shortening the run time from days to hours.

The output spectrum of this new X-ray beam can be seen in Figure 6 as well as the documented spectrum from the manufacturer. Above 75 keV the spectra shape matches relatively well, however, below this the intensity of the simulated spectrum is slightly higher. The characteristic X-ray peaks near ~10, ~60, and ~70 keV match between both simulations, however, the higher overall intensity in this region is due to some inherent aluminum filtration present in the manufacturer spectrum. We elected to include these features in the main VIP-man simulation where different filters and collimation/tube head designs can be iterated. This low energy region will be filtered out, in order to flatten the beam profile.

To calculate dose, we used an F6 tally to determine the energy deposition in MeV/g for a given tissue of interest. Due to some limitations of MCNP, it is unable to sum the mass of all voxels with the same tissue type, leaving the results in MeV. Dividing by the number of voxels of each tissue type resolves this issue as instructed by comments in the VIP-man documentation. However, in MCNP the tally results are also normalized to one source particle. The number of photons produced is dependent upon the number of electrons striking the target in the simple X-ray tube simulation. The number of electrons depends on the X-ray tube current, in this case 3 mA. Equation 4 relates the number of electrons to the number of photons produced in the VIP-man simulation while Equation 5 relates the number of photons to dose rate in Gy/s. These two equations allow for the conversion between the known electron production rate and the simulated X-ray output from the simulation.

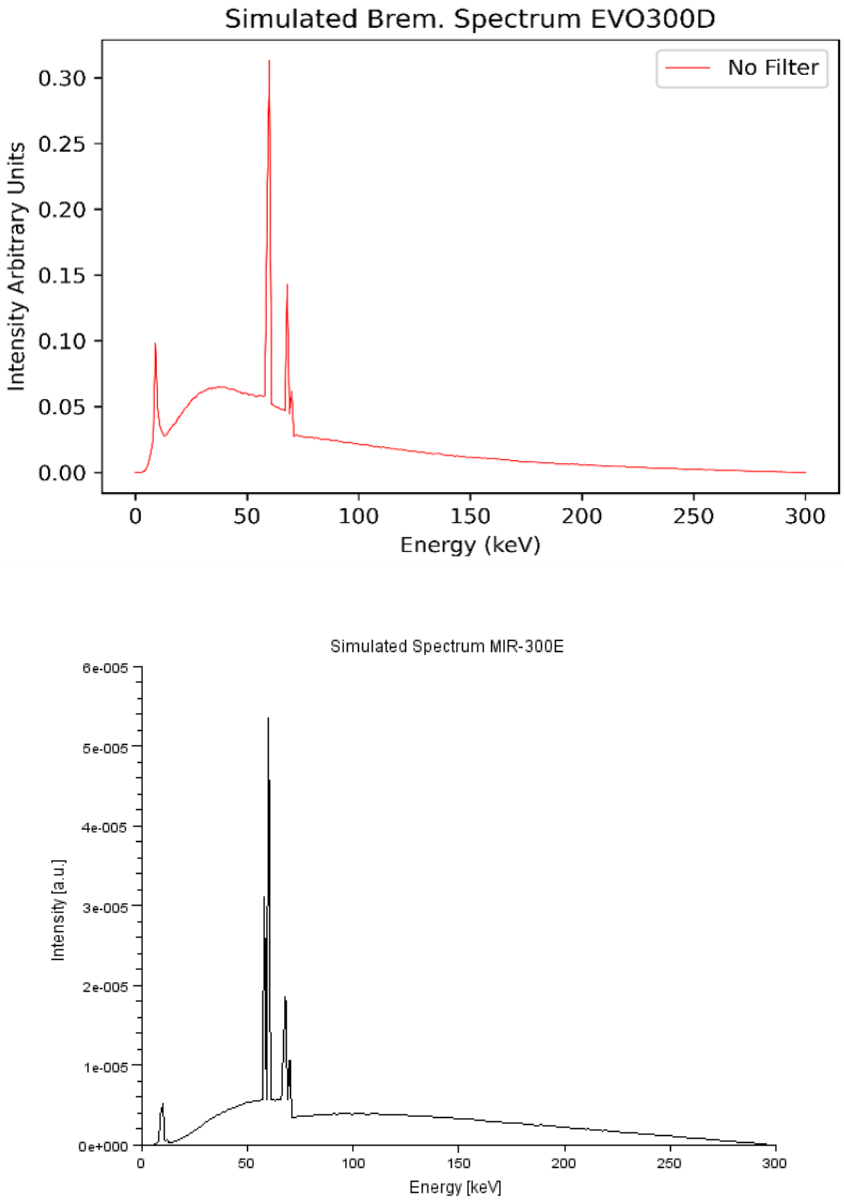

Figure 6. The top image is the MCNP simulated X-ray spectrum the bottom image is the simulated X-ray spectrum from the manufacturer. Both spectra are plots of intensity in arbitrary units versus energy in keV.

$$nps = Tube\ Current \times Ampere \times Xray\ Production\ Factor \quad (4)$$

$$Dose\ rate = \frac{nps \times F6\ tally \times MeV\ to\ Joules \times Kg}{Number\ of\ Voxels} \quad (5)$$

Tube current is given in mA and one ampere is 6.242E18 electrons per second. The X-ray production factor describes how many X-rays are produced in the 27º half angle cone per electron. This product gives nps, the number of photons produced by the X-ray tube per second. The dose rate (Gy/s) is found by multiplying nps with the F6 tally results in MeV and converting to Joules with the conversion factor, 1.602E-13. Multiplying by 1,000 converts this result from grams to kilograms. By finally dividing by the number of voxels, the dose rate to any tissue can be determined.

To quantify the dose as a function of depth in the lungs, some modifications had to be made to the VIP-man phantom. We used a custom python script to parse the (X,Y,Z) position values of lung voxels in the VIP-man input deck. The Y-axis corresponds to the axis parallel to the beam, the X-axis lateral to the body and the Z-axis running superior/inferior. For each Y position starting at the anterior of the lungs, all lung voxels in the X and Z directions were given a new cell ID number in the simulation. Then a new cell ID was created corresponding to that layer as well as a new F6 tally. The number of voxels corresponding to each layer was also determined so the dose calculation can be normalized. This modification divided the lungs into 49 layers in the Y direction as shown in Figure 7, so that dose as a function of depth can be determined. Figure 8 shows the dose vs. depth in the lungs as a function of distance into the body for both the simulated X-ray cone and for a full electron/target/X-ray source.

The slight variation in the curves can be attributed to less-than-ideal convergence for the full bremsstrahlung simulation with some of the statistical checks for the tallies not passing. Still, with these issues the two curves match very closely, verifying that the bremsstrahlung conversion factor from Equation 4, and the weighting factor in the X-ray cone simulation were correct. The improved simulation speed also improves iteration time with different collimators or filters.

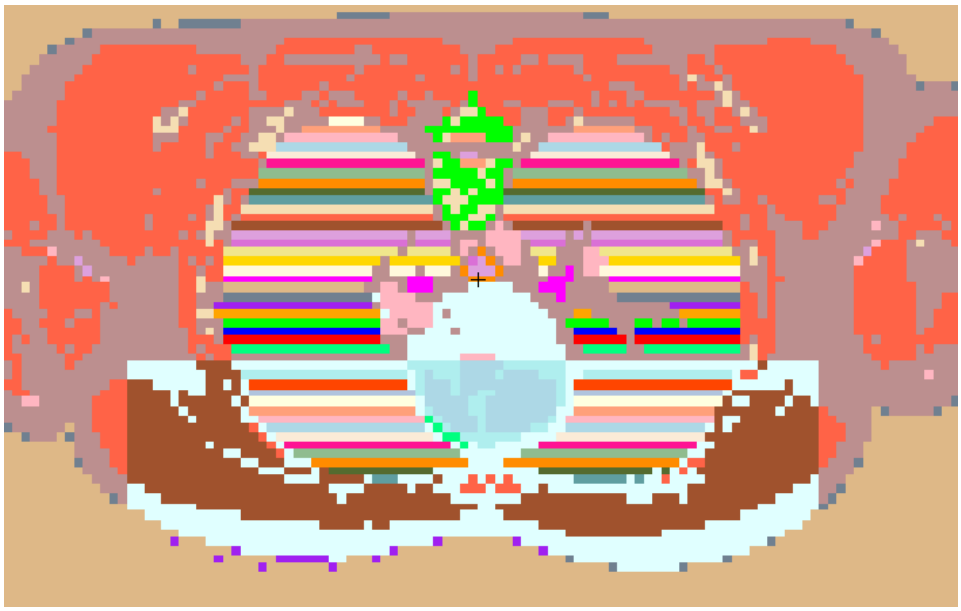

Figure 7. VIP-man transverse cross-section at the mid chest level. The color scheme is randomly assigned by the MCNP built in visualization tool. The heart (center white) and chest wall (dark and light red around the peripheral) are clearly distinguishable. The left to right, equally spaced stripes correspond to each layer of lung tissue for depth curves. The X-ray source would be located out of frame to the bottom directed upwards toward the chest wall.

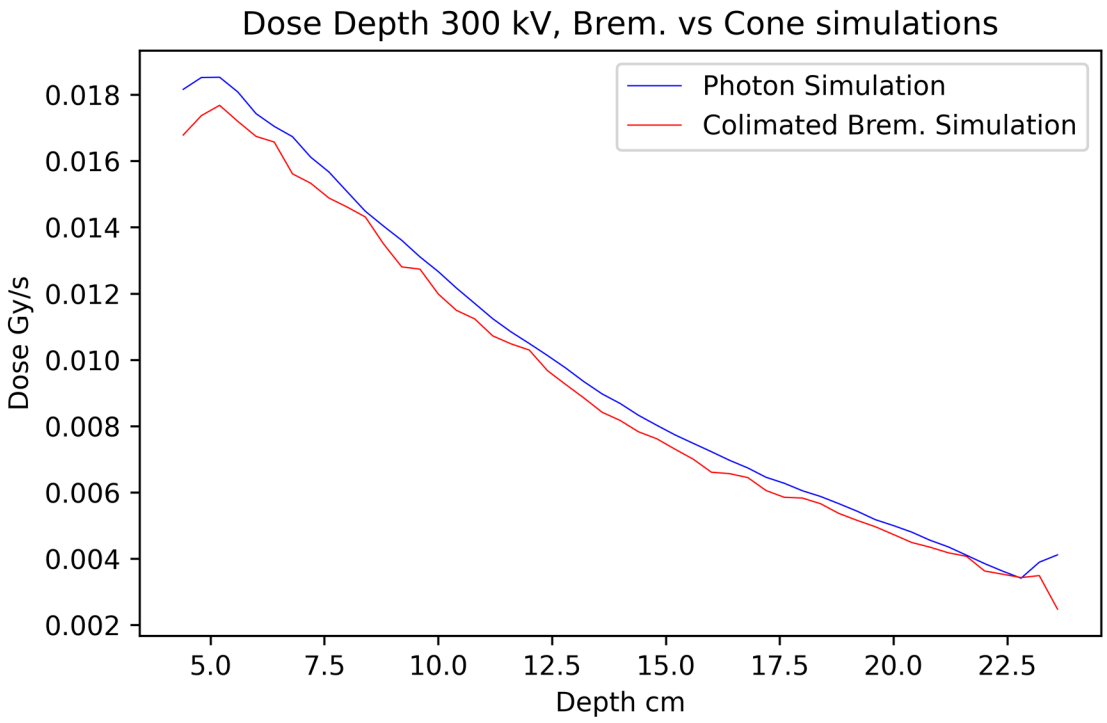

Figure 8. Dose rate versus depth curves as a function of depth into the body in cm for the X-ray cone simulation (Blue) and the full electron/target/X-ray simulation (Red). The slight variation with the collimated bremsstrahlung spectrum can be attributed to poor convergence and some failed statistical checks even after long simulation times.

3.2 Filter Design

The unfiltered X-ray spectrum shows a steep dose gradient from the front to back of the lungs. Not shown in Figure 8. is the higher dose rate to the front of the chest wall, skin, and other tissues. By hardening the beam with the addition of a filter, the dose rate will be more uniform with depth. Material selection is important for a filter due to characteristic X-ray production and attenuation. A Thoraeus filter is comprised of tin, copper, and aluminum [55]. This hardens the beam while each successive layer attenuates the characteristic X-rays of the previous layer. This design is more efficient than a filter of a single material type. Common material thicknesses for 200 – 400 keV X-ray tubes are 1.2 mm of Tin, 0.25 mm of copper, and 1 mm of aluminum. Figure 9 compares the Thoraeus filtered spectrum with the unfiltered photon beam spectrum showing a slight decrease in high energy X-rays with a substantial decrease in X-ray intensity below ~130 keV. It is important to note that increasing filter thickness decreases the total X-ray intensity, therefore dose rate. Figure 10 shows how this filter compares to a 4 mm solid Copper filter in flattening the dose depth curve.

Another factor contributing to the steep dose gradient with distance is the short source to surface distance (SSD) of 35 cm. This was chosen due to the large opening angle of the collimator allowing us to take advantage of the $1/r^2$ relationship between dose rate and distance to the source, r. This shortens the treatment time and reduces the flux by about 50% due to beam divergence through the body.

To calculate the treatment time, and therefore total dose delivered to the lungs, skin, and heart, the lung plane 26 was chosen as it is roughly the center of the lungs. The prescribed dose at isocenter of 1.5 Gy divided by the dose rate at this layer gives the treatment time in seconds for each setup. Table 1 contains the dose, dose rates, and treatment times for filtered and unfiltered anterior-posterior (AP) beams.

The addition of filters nearly doubled the treatment time due to the decrease in beam output across all energies. The marginal improvement of the skin dose suggests that the low energy X-ray flux is still high enough to cause a substantial entrance dose. However, the shallow slope of the filtered lung dose curve shows improved uniformity with depth.

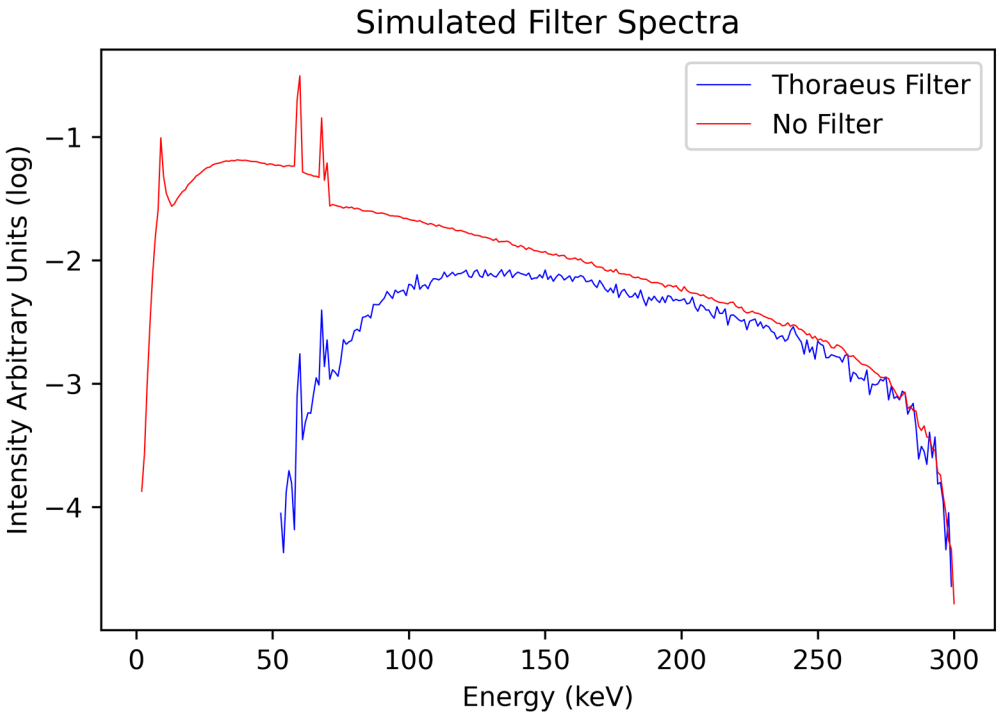

Figure 9. Log scale of X-ray intensity vs X-ray energy in keV for an unfiltered photon beam and a Thoraeus filtered photon beam. The intensity below ~130 is many times lower with the filter while only slightly lower at the higher energies.

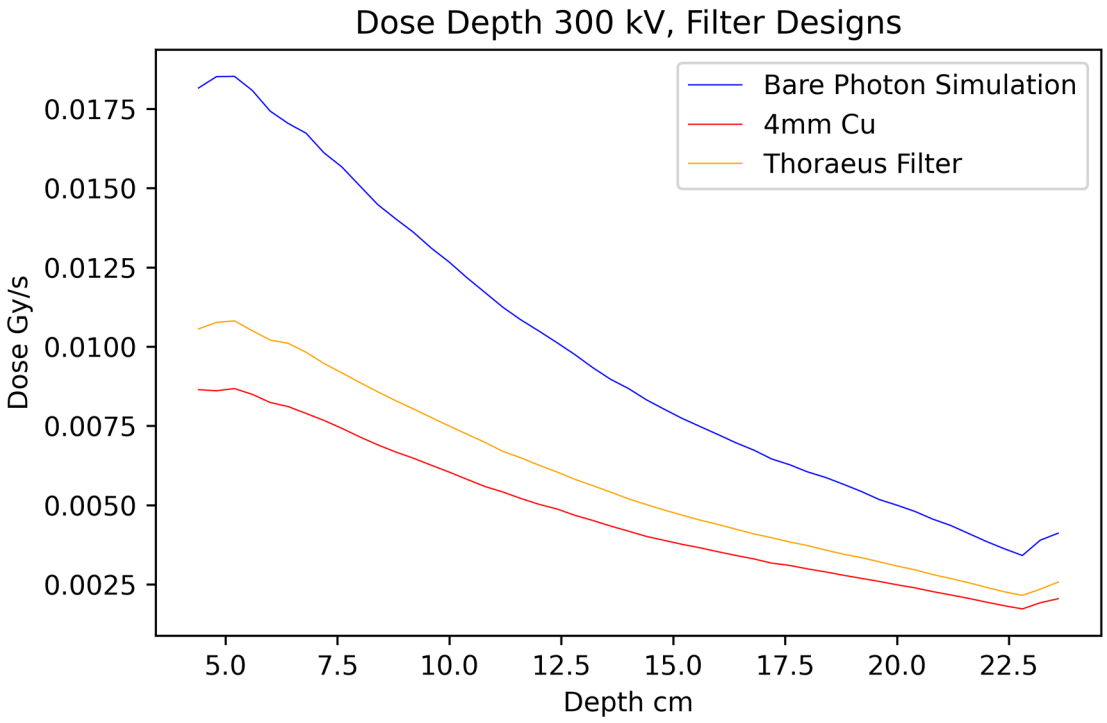

Figure 10. Dose rate vs depth in lungs for an unfiltered photon beam, a Thoraeus filtered beam, and a 4 mm Copper filtered beam for comparison. Note the shallower slope of the filtered beams compared to the unfiltered beam showing improve dose uniformity.

Table 1. Dose, dose rate, and treatment times for organs of interest.

Filter Type	**Skin Rate**	**Skin Dose**	**Heart Rate**	**Heart Dose**	**Lung Rate**	**Lung Dose**	**Time**
Photon simulation	1.77 cGy/s	297 cGy	0.84 cGy/s	140 cGy	0.84 cGy/s	140 cGy	167 s
Thoraeus filter	1.0 cGy/s	288 cGy	0.5 cGy/s	137 cGy	0.50 cGy/s	140 cGy	277 s
4mm Cu filter	0.84 cGy/s	292 cGy	0.4 cGy/s	138 cGy	0.41 cGy/s	140 cGy	345 s

3.3 Parallel Apposing Fields

As shown in Figure 7, the MCNP visual representation of VIP-man cross sections are unable to display dose information in a useful way. To solve this a Python script was developed to parse the input deck and determine the voxel material type, ID, and density for each (X,Y,Z) position. With this, cross sectional views of each plane can be plotted for better visualization with custom color maps. With commercial treatment planning software, dose overlays are placed on CT-scans of the anatomy which are represented in Hounsfield Units or HU. These are calculated with Equation 6 and depend on the measured attenuation coefficient of X-rays through a given voxel in the body in reference to the attenuation coefficient of water [63].

The attenuation coefficient of a material is equal to the electron density times the cross sections for photo electric, coherent and incoherent scattering. If we assume that the electron density and cross sections of all tissues are roughly equivalent, then mass density can be substituted for the attenuation coefficient in Equation 7.

$$HU = \left(\frac{\mu_{tissue} - \mu_{water}}{\mu_{water}}\right) \times 1{,}000 \tag{6}$$

To calculate HU or CT number, the attenuation through a voxel μ_{tissue} is subtracted from the attenuation coefficient for water μ_{water}, and finally divided by the attenuation coefficient for water, μ_{water} and multiplied by 1,000. This means that pure water would have an HU value of 0 with all other tissues scaling from that point.

$$HU' = \left(\frac{\rho_{tissue} - \rho_{water}}{\rho_{water}}\right) \times 1{,}000 \tag{7}$$

By replacing μ with density, ρ, any tissue with a density equal to the density of water would still have an HU′ of 0. With this correction, applying a grayscale to the HU′ values gives roughly the same contrast as a CT scan.

Now the corresponding (X,Y,Z) tally results for lung tissue must be determined in simulation to represent the dose distribution at different cross-sectional layers. Again, due to some memory limitations of MCNP, the entire lung volume could not be read out in a single simulation. So, F6 tally results could only be generated for a single cross-sectional plane at a time in each simulation run. Once this was generated, the positional dose per voxel was calculated using Equation 5, and overlayed with the approximated CT scan for the 2-D dose distribution seen in Figure 11. The same process was repeated for the coronal plane in Figure 12.

Next, a posterior-anterior (PA) beam was simulated with the same SSD distance of 35 cm to the back of the phantom with the same isocenter. This gives another dose distribution map for comparison with the previous beam geometry which can be seen in Figure 13. This distribution leads us to believe that a PA field setup performs slightly better due to the location of the heart when compared to the anterior-posterior (AP) field. With a majority of the lung tissue posterior to the heart, there is less attenuation of the beam through the centerline.

To increase dose uniformity, these two fields were combined and weighted individually to achieve the most uniform dose distribution through the lung volume. The resulting weights were 0.35 AP and 0.65 PA meaning that weighting the beam towards the back improved the lung dose coverage shown in Figure 14. If we consider the attenuation of the beam to be similar through the chest and the back walls, the heart would be the major contributor to this difference in weighting. Figure 15 also shows improved dose uniformity over the coronal plane at isocenter. It is apparent from Figures 14 and 15 that opposing AP and PA fields, weighted correctly, further improve the dose distribution to the lungs.

Unfortunately, skin entrance dose was not tallied correctly for the PA beam and reported total skin dose across the entire body. In order to accurately determine the dose to the chest and back, the VIP-man phantom would need to be further modified since dose is tallied across the total skin volume, not just the area in the beam. However, by applying the beam weights to the skin dose from the AP beam, we can estimate that the back and chest would receive approximately 1.8 and 1 Gy, respectively.

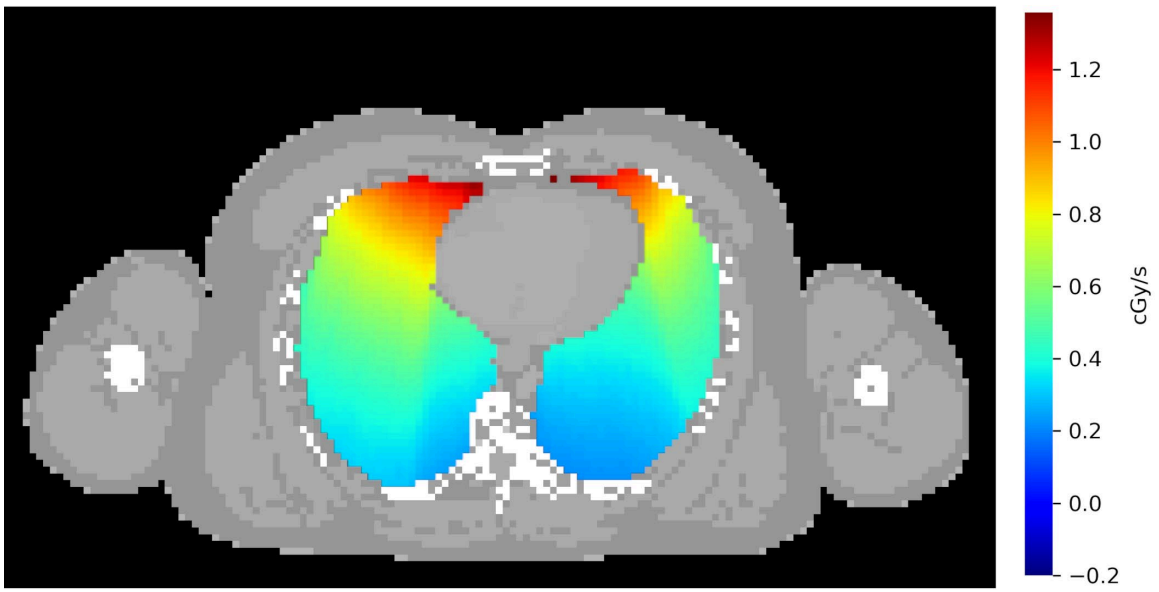

Figure 11. A transverse plane view at isocenter with an AP beam and a lung dose overlay.

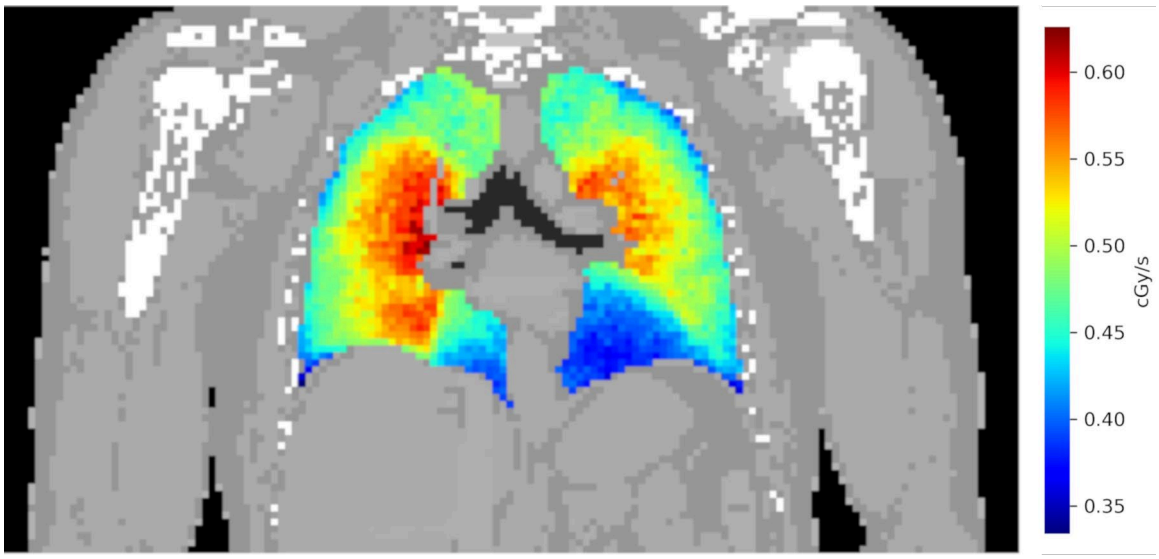

Figure 12. A coronal plane view at isocenter with the dose to the lungs overlayed.

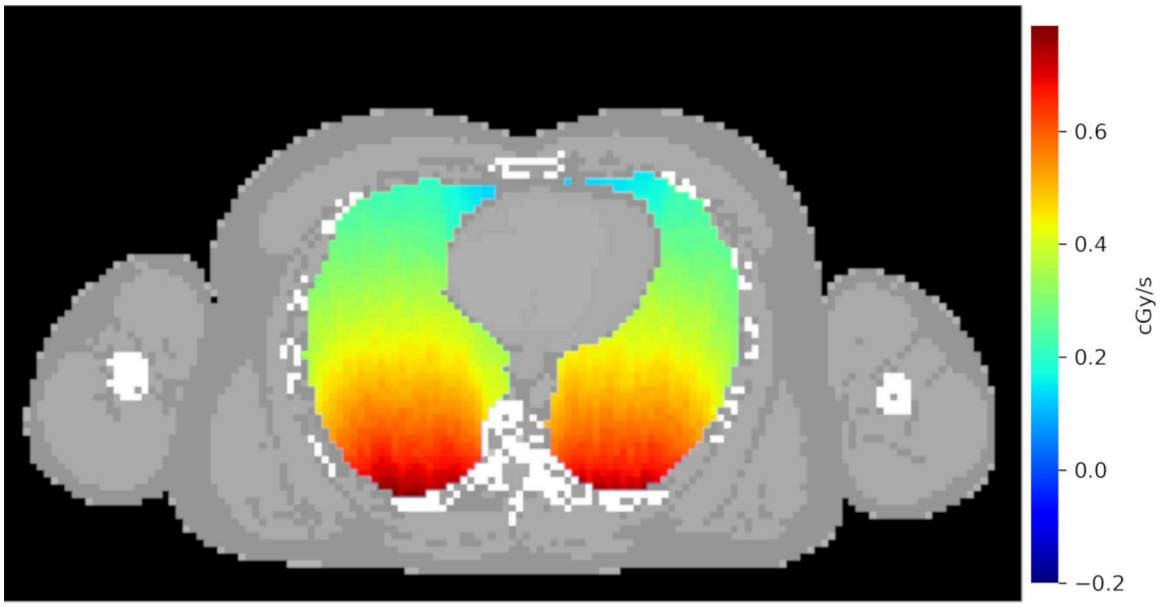

Figure 13. A transverse plane view at isocenter of the dose to the lungs with a PA beam setup.

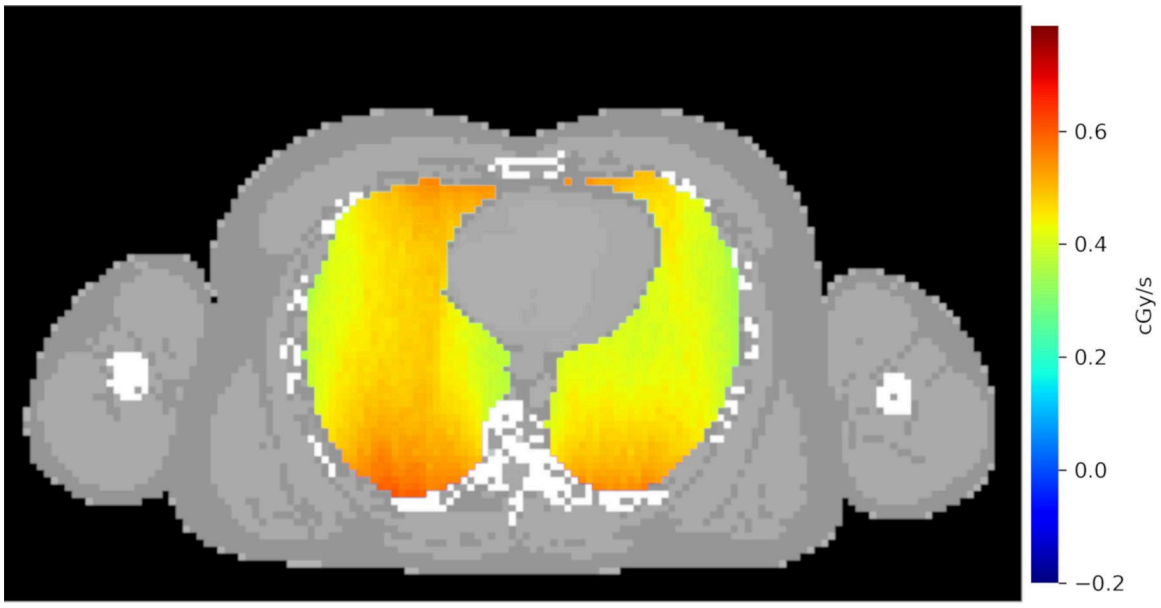

Figure 14. A transverse plane view at isocenter with a 0.35 AP, 0.65 PA beam weighting resulting in a very uniform dose distribution.

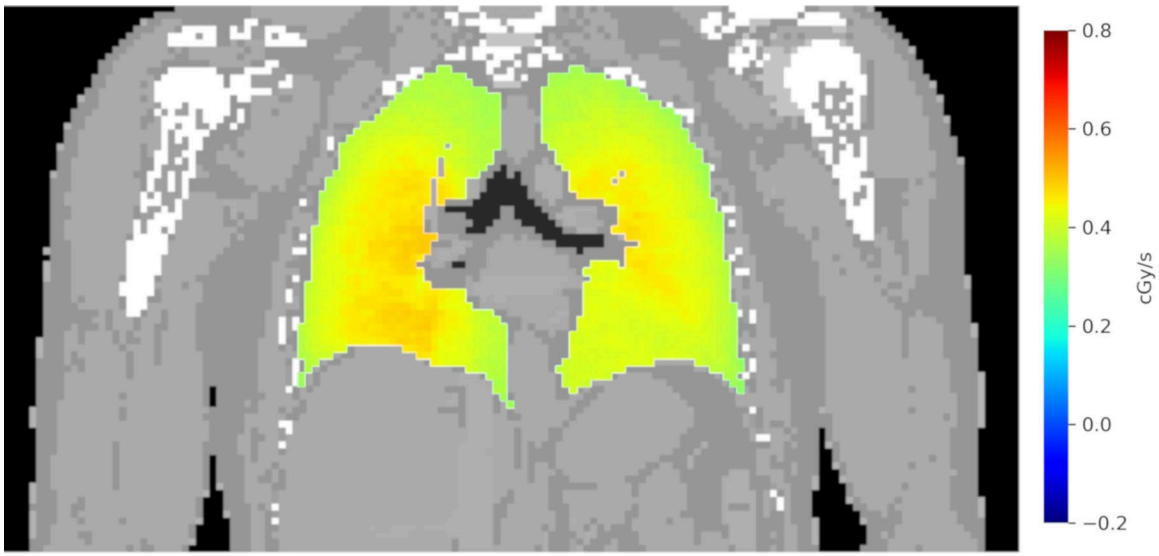

Figure 15. A coronal plane view at isocenter with a 0.35 AP, 0.65 PA beam weighting.

Additional field setups could be investigated to spread the entrance dose over a greater area. Focusing the beam on one individual lung at a time from orthogonal directions could further improve dose uniformity. This would also allow for tighter collimation of the beam, improving the dose depth profile due to less beam divergence. This would come at the cost of prolonged treatment time, past the ~5 minutes of the current method.

CHAPTER FOUR

FUTURE WORK

4.1 Radiation Enclosure

Since the X-ray tube chosen for this work is capable of high dose rates, steps must be taken in order to test its capabilities safely. This will require the design, building, and testing of a radiation enclosure rated to contain the 300 kVp source at maximum output while meeting all state and federal regulations. One such enclosure has been selected which was previously rated for a 160 kVp tube. With the aid of MCNP and NCRP report calculations, we will determine the amount of additional lead shielding that must be added. This will involve fabrication of lead panels and reengineering the safety locks.

4.2 Beam Verification and Dosimetry

Using the radiation enclosure, the X-ray beam will be measured for both uniformity and output. With this data, the MCNP beam model can be updated if there are any discrepancies in output. This will be further refined with the use of a human tissue equivalent phantom. By placing TLDs inside the phantom, the dose rate to each location within the phantom can be experimentally verified with the calibrated TLDs.

4.3 2D-Planning

Due to the simple nature of the X-ray fields, we will experiment with the possibility of using dose depth curves and physical measurements of the phantom to calculate the dose deposition to the lungs. This would forgo the necessity of using a CT-scan prior to planning to determine the exposure duration and field weighting. These calculations will be verified with an updated MCNP model and experimentally determined for variables, such as body mass.

LIST OF REFERENCES

1. Gianfaldoni, S., et al., *An Overview on Radiotherapy: From Its History to Its Current Applications in Dermatology.* Open Access Maced J Med Sci, 2017. **5**(4): p. 521-525.
2. Hess, C.B., et al., *Low-Dose Whole-Lung Radiation for COVID-19 Pneumonia: Planned Day-7 Interim Analysis of an Ongoing Clinical Trial.* medRxiv, 2020: p. 2020.06.03.20116988.
3. Hess, C.B., et al., *Immunomodulatory Low-Dose Whole-Lung Radiation for Patients with Coronavirus Disease 2019-Related Pneumonia.* Int J Radiat Oncol Biol Phys, 2021. **109**(4): p. 867-879.
4. Lara, P.C., J. Burgos, and D. Macias, *Low dose lung radiotherapy for COVID-19 pneumonia. The rationale for a cost-effective anti-inflammatory treatment.* Clinical and Translational Radiation Oncology, 2020. **23**: p. 27-29.
5. Matthay, M.A., L.B. Ware, and G.A. Zimmerman, *The acute respiratory distress syndrome.* The Journal of Clinical Investigation, 2012. **122**(8): p. 2731-2740.
6. Assmus, A., *Early history of X rays.* Beam Line, 1995. **25**(2): p. 10-24.
7. Grubbé, E.H., *Priority in the therapeutic use of X-rays.* Radiology, 1933. **21**(2): p. 156-162.
8. Becquerel, H. and P. Curie, *Action physiologique des rayons du radium.* Compt. Rend. Acad. Sci, 1901. **132**: p. 1289-1291.
9. Musser, J. and D. Edsall, *A study of metabolism in leukaemia, under the influence of the x-ray.* Tr A Am Physicians, 1905. **20**: p. 294-323.
10. Quimby, A.J. and W.A. Quimby, *Unresolved pneumonia: successful treatment by Röngen Ray*. 1916: AR Elliott.
11. Lawrence, E.O. and M.S. Livingston, *The production of high speed light ions without the use of high voltages.* Physical Review, 1932. **40**(1): p. 19.
12. Heidenhain, L. and C. Fried, *Röntgenstrahlen und Entzündung.* Klinische Wochenschrift, 1924. **3**(25): p. 1121-1122.
13. Calabrese, E.J. and G. Dhawan, *How radiotherapy was historically used to treat pneumonia: could it be useful today?* Yale J Biol Med, 2013. **86**(4): p. 555-70.
14. Muller, H.J., *The production of mutations by X-rays.* Proceedings of the National Academy of Sciences, 1928. **14**(9): p. 714-726.
15. Coutard, H., *Principles of x ray therapy of malignant diseases.* The lancet, 1934. **224**(5784): p. 1-8.
16. Tsien, K. and R. Robbins, *A Comparison of a Cobalt-60 Teletherapy Unit and a 2-MEV Van de Graaff X-ray Generator on the Basis of Physical Measurements.* Radiology, 1958. **70**(4): p. 486-502.
17. Pereira, G.C., M. Traughber, and R.F. Muzic, Jr., *The role of imaging in radiation therapy planning: past, present, and future.* Biomed Res Int, 2014. **2014**: p. 231090.
18. Van Dyk, J., J.J. Battista, and P. Almond, *A retrospective of Cobalt-60 radiation therapy:"The atom bomb that saves lives".* Med. Phys Int J, 2020. **4**.

19. Thwaites, D.I. and J.B. Tuohy, *Back to the future: the history and development of the clinical linear accelerator.* Physics in medicine & biology, 2006. **51**(13): p. R343-R362.
20. Martins, P.N., *A brief history about radiotherapy.* International Journal of Latest Research in Engineering and Technology (IJLRET), 2018. **4**: p. 08-11.
21. Do Huh, H. and S. Kim, *History of radiation therapy technology.* Progress in Medical Physics, 2020. **31**(3): p. 124-134.
22. Thompson, B.T., R.C. Chambers, and K.D. Liu, *Acute Respiratory Distress Syndrome.* New England Journal of Medicine, 2017. **377**(6): p. 562-572.
23. Bellani, G., et al., *Epidemiology, Patterns of Care, and Mortality for Patients With Acute Respiratory Distress Syndrome in Intensive Care Units in 50 Countries.* JAMA, 2016. **315**(8): p. 788-800.
24. Auld, S.C., et al., *ICU and Ventilator Mortality Among Critically Ill Adults With Coronavirus Disease 2019.* Crit Care Med, 2020. **48**(9): p. e799-e804.
25. Calabrese, E.J., et al., *Nrf2 activation putatively mediates clinical benefits of low-dose radiotherapy in COVID-19 pneumonia and acute respiratory distress syndrome (ARDS): Novel mechanistic considerations.* Radiotherapy and Oncology, 2021. **160**: p. 125-131.
26. Ameri, A., et al., *Low-Dose Whole-Lung Irradiation for COVID-19 Pneumonia: Short Course Results.* Int J Radiat Oncol Biol Phys, 2020. **108**(5): p. 1134-1139.
27. Sanmamed, N., et al., *Low-Dose Radiation Therapy in the Management of Coronavirus Disease 2019 (COVID-19) Pneumonia (LOWRAD-Cov19): Preliminary Report.* Int J Radiat Oncol Biol Phys, 2021. **109**(4): p. 880-885.
28. Meziani, L., et al., *Low Doses of Radiation Increase the Immunosuppressive Profile of Lung Macrophages During Viral Infection and Pneumonia.* International Journal of Radiation Oncology*Biology*Physics, 2021. **110**(5): p. 1283-1294.
29. Thwaites, D.I. and J.B. Tuohy, *Back to the future: the history and development of the clinical linear accelerator.* Physics in Medicine & Biology, 2006. **51**(13): p. R343.
30. Molina, J.R., et al., *Non-Small Cell Lung Cancer: Epidemiology, Risk Factors, Treatment, and Survivorship.* Mayo Clinic Proceedings, 2008. **83**(5): p. 584-594.
31. Sale, C. and P. Moloney, *Dose comparisons for conformal, IMRT and VMAT prostate plans.* Journal of Medical Imaging and Radiation Oncology, 2011. **55**(6): p. 611-621.
32. Ballas, L.K., et al., *Radiation therapy facilities in the United States.* Int J Radiat Oncol Biol Phys, 2006. **66**(4): p. 1204-11.
33. Dracham, C.B., A. Shankar, and R. Madan, *Radiation induced secondary malignancies: a review article.* Radiat Oncol J, 2018. **36**(2): p. 85-94.
34. Armstrong, G.T., et al., *Late mortality among 5-year survivors of childhood cancer: a summary from the Childhood Cancer Survivor Study.* J Clin Oncol, 2009. **27**(14): p. 2328-38.
35. Berrington de Gonzalez, A., et al., *Second Solid Cancers After Radiation Therapy: A Systematic Review of the Epidemiologic Studies of the Radiation*

Dose-Response Relationship. International Journal of Radiation Oncology*Biology*Physics, 2013. **86**(2): p. 224-233.
36. Boice Jr, J.D., et al., *Introduction to the special issue on the US Million Person Study of health effects from low-level exposure to radiation.* International journal of radiation biology, 2022. **98**(4): p. 529-532.
37. Boice Jr, J.D. and L.T. Dauer, *Million Person Study of Low-Dose Radiation Health Effects.* Nuclear Science and Engineering, 2022.
38. Nrc. *Gray (Gy)*. 2022 [cited 2022 11/10]; Available from: https://www.nrc.gov/reading-rm/basic-ref/glossary/gray-gy.html.
39. Einstein, A., *The photoelectric effect.* Ann. Phys, 1905. **17**(132): p. 4.
40. Britannica, T.E.o.E., *"Compton effect"*, in *Encyclopedia Britannica*. 2022, @britannica.
41. jfk. *II X-rays for Diagnosis*. 1995 [cited 2022 10/7]; Available from: http://img.chem.ucl.ac.uk/www/kelly/medicalxrays.htm.
42. Sia, J., et al., *Molecular Mechanisms of Radiation-Induced Cancer Cell Death: A Primer.* Frontiers in Cell and Developmental Biology, 2020. **8**.
43. Borek, C., *Antioxidants and Radiation Therapy.* The Journal of Nutrition, 2004. **134**(11): p. 3207S-3209S.
44. Hubbell, J.H., *Photon mass attenuation and energy-absorption coefficients.* The International Journal of Applied Radiation and Isotopes, 1982. **33**(11): p. 1269-1290.
45. *NIST: X-Ray Mass Attenuation Coefficients - Water, Liquid*. 2022 [cited 2022 10/3]; Available from: https://physics.nist.gov/PhysRefData/XrayMassCoef/ComTab/water.html.
46. Nadrljanski, M.M., *X-ray tube | Radiology Reference Article | Radiopaedia.org.* 2022.
47. McCollough, C.H., *The AAPM/RSNA physics tutorial for residents. X-ray production.* RadioGraphics, 1997. **17**(4): p. 967-984.
48. Hahn, C., et al., *First observation of signals due to KAERI's 10 MeV electron beam by using GEM detectors.* Journal of The Korean Physical Society - J KOREAN PHYS SOC, 2007. **50**.
49. Omar, A., P. Andreo, and G. Poludniowski, *A model for the energy and angular distribution of x rays emitted from an x-ray tube. Part I. Bremsstrahlung production.* Medical Physics, 2020. **47**(10): p. 4763-4774.
50. *Bremsstrahlung Radiation - PhysicsOpenLab.* 2022.
51. *X-ray_tube*. 2022 [cited 2022 11/14]; Available from: https://www.bionity.com/en/encyclopedia/X-ray_tube.html.
52. Allard, D., *WE-H-204-01: William D. Coolidge, Inventor of the Modern X-Ray Tube.* Medical Physics, 2016. **43**(6Part42): p. 3838-3839.
53. Shaik, A. *Thermionic emission*. 2022; Available from: https://www.physics-and-radio-electronics.com/electronic-devices-and-circuits/electron-emission/thermionicemission.html.

54. Rana, N., et al., *Evaluation of external beam hardening filters on image quality of computed tomography and single photon emission computed tomography/computed tomography.* J Med Phys, 2015. **40**(4): p. 198-206.
55. Trout, E., J. Kelley, and A. Lucas, *Evaluation of Thoraeus filters.* The American journal of roentgenology, radium therapy, and nuclear medicine, 1961. **85**: p. 933-939.
56. Ahnesjö, A., M. Saxner, and A. Trepp, *A pencil beam model for photon dose calculation.* Medical Physics, 1992. **19**(2): p. 263-273.
57. Starkschall, G., et al., *Beam-commissioning methodology for a three-dimensional convolution/superposition photon dose algorithm.* Journal of Applied Clinical Medical Physics, 2000. **1**(1): p. 8-27.
58. Ahnesjö, A. and M.M. Aspradakis, *Dose calculations for external photon beams in radiotherapy.* Phys Med Biol, 1999. **44**(11): p. R99-155.
59. Reynaert, N., et al., *Monte Carlo treatment planning for photon and electron beams.* Radiation Physics and Chemistry, 2007. **76**(4): p. 643-686.
60. Rogers, D. and A. Bielajew, *Monte Carlo techniques of electron and photon transport for radiation dosimetry.* The dosimetry of ionizing radiation, 1990. **3**: p. 427-539.
61. Shultis, J.K. and R.E. Faw, *An MCNP primer*. 2011.
62. Xu, X.G., T.C. Chao, and A. Bozkurt, *VIP-MAN: AN IMAGE-BASED WHOLE-BODY ADULT MALE MODEL CONSTRUCTED FROM COLOR PHOTOGRAPHS OF THE VISIBLE HUMAN PROJECT FOR MULTI-PARTICLE MONTE CARLO CALCULATIONS.* Health Physics, 2000. **78**(5).
63. Schneider, U., E. Pedroni, and A. Lomax, *The calibration of CT Hounsfield units for radiotherapy treatment planning.* Physics in Medicine & Biology, 1996. **41**(1): p. 111.
64. OncologyMedicalPhysics. *Linear Accelerator Basics | Oncology Medical Physics*. 2022; Available from: https://oncologymedicalphysics.com/introduction-to-clinical-linear-accelerators/.
65. Leal, A., et al., *MLC leaf width impact on the clinical dose distribution: a Monte Carlo approach.* International Journal of Radiation Oncology*Biology*Physics, 2004. **59**(5): p. 1548-1559.
66. Sterzing, F., et al., *Image-guided radiotherapy: a new dimension in radiation oncology.* Dtsch Arztebl Int, 2011. **108**(16): p. 274-80.

APPENDIX

Linac Operational Features

Modern linacs function using the same principles as X-ray tubes, accelerating electrons into a high-Z target to produce bremsstrahlung radiation. However, linacs use a different method of accelerating electrons to reach much higher energies. They are heavily optimized for cancer therapy and tumor coverage at a variety of depths which is why high energies are an important feature of their design. They are much more complex devices; therefore, this section will only discuss the key differences of their design.

Linacs use a different method of electron acceleration involving microwave resonances. By using a klystron or magnetron, high frequency electro-magnetic waves (microwaves) are produced [64]. These microwaves are then directed into a device called a wave guide which is a metal tube with many chambers for the microwaves to resonate in. Electrons are introduced into this tube by an electron gun which uses thermionic emission like in the X-ray tube to produce free electrons. The electrons ride these resonance waves inside of the tube to accelerate to very high speeds, anywhere from 2-18 MeV, depending on the design. They then strike a dense high-Z target to produce bremsstrahlung radiation, just like an X-ray tube. However, linacs are designed to have their X-ray beam port in line with the electron beam to take advantage of the hugely forward directed radiation in the MeV energy ranges [48, 64]. This design requires multiple target thicknesses for different energies as well as complex cooling systems and electron beam steering to ensure proper output. Today, complex multi-leaf collimators can be used to manipulate the X-ray beam to nearly any shape imaginable for the purposes of target tissue coverage [65]. One other feature that is not present with X-ray tubes is the ability to remove the X-ray target and allow the electron beam to be used for treatment.

With multileaf collimator (MLC) leaves and the ability to adapt the X-ray output in real time, advanced forms of treatment are possible such as IMRT and VMAT [31]. Advanced algorithms can modulate the MLC configuration and beam output to create highly conformal dose distributions around the target structures. With the addition of

IGRT, onboard imaging can track specified locations to automatically gate the beam output [66]. These specialized features have made linacs effective at delivering high dose rate therapy to precise locations inside the body.

VITA

Thomas “Heath” Davis was born in Asheville, North Carolina, on February 1st, 1998. They graduated from North Buncombe High School with honors in May 2016. The following August they entered The University of Tennessee and in 2020 received Bachelor of Science in Nuclear Engineering. They stayed at the University of Tennessee to pursue a Master of Science Degree in Medical Physics in December 2022.